

Received 16 June 2025, accepted 11 July 2025, date of publication 14 July 2025, date of current version 23 July 2025.

Digital Object Identifier 10.1109/ACCESS.2025.3588913



RESEARCH ARTICLE

System-Level Assessment of Shaped Elevation Beam Patterns for Hybrid Beamforming in mm-Wave 5G Networks With Spatially Heterogeneous Traffic

WENXU CHEN[®]¹, YANKI ASLAN[®]¹, REMCO LITJENS[®]^{2,3}, AND ALEXANDER YAROVOY¹, (Fellow, IEEE)

Corresponding author: Yanki Aslan (Y.Aslan@tudelft.nl)

ABSTRACT The throughput performance of intelligently shaped and fixed analog elevation beam patterns in millimeter-wave (mm-wave) base stations with hybrid beamforming (HBF) is assessed for the first time. Distinct spatially heterogeneous user distributions (i.e., uniform, near-site, cell-edge, and weighted uniform and near-site) and propagation environments (i.e., line-of-sight (LoS) with multipath and non-line-of-sight (NLoS) with multipath) are considered. The cosecant-squared and flat-top shaped beam patterns are compared to the benchmark pencil beam pattern with a straightforward electrical downtilt. The LoS simulation results show that in case of unknown weight of user distribution scenarios, the cosecant-squared pattern is the most robust, with a gain of up to 16% in the average system throughput and up to 34% in the 90th percentile user throughout compared to the benchmark. If the near-site case has a greater probability of occurrence than the uniform user distribution (e.g., due to daily events and festivals), the flat-top pattern becomes preferable. In the NLoS scenario, the considered HBF architectures with elevation beam pattern shaping do not bring any performance disadvantages compared to the benchmark HBF.

INDEX TERMS 5G, base station antennas, hybrid beamforming, millimeter-waves, phased arrays, throughput performance.

I. INTRODUCTION

The 5th generation (5G) mobile network technology (and beyond) promises to revolutionize and connect the global world through seamless connectivity [1]. Driven by inevitably increasing demand for mobile data transmission and very limited available spectrum resources, the 5G wireless systems consider the utilization of millimeter wave (mm-wave) frequency bands. It is known that at high-frequency bands (e.g., frequency range 2 (FR2) at frequencies of 24 GHz and higher), the electromagnetic wave suffers from severe

The associate editor coordinating the review of this manuscript and approving it for publication was Wanchen Yang .

propagation losses and potential signal blockage, which substantially degrades the signal-to-interference-plus-noise ratio (SINR) and thus leads to lower bit rates [2]. To compensate for that and to enhance the throughput and coverage, massive multiple-input multiple-output (mMIMO) transmission serves as the key enabling technology. The mMIMO technology allows antenna arrays to transmit multiple layers to the user equipment (UE) by utilizing a large number of antenna elements that operate fully coherently and adaptively. Beamforming is performed in downlink and uplink communications, which involves the signal processing procedure before transmitting (i.e., precoding) and after receiving (i.e., combining or detecting) data streams. This

¹Microwave Sensing, Signals and Systems Group, Department of Microelectronics, Delft University of Technology, 2628 CD Delft, The Netherlands

²Department of Networks, TNO, 2595 DA The Hague, The Netherlands

³Network Architectures and Services Group, Department of Quantum and Computer Engineering, Delft University of Technology, 2628 CD Delft, The Netherlands



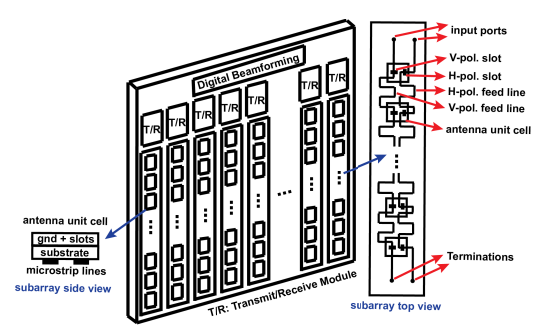


FIGURE 1. A sample base station HBF array structure with dual-polarized vertical subrarrays. Possible implementations are demonstrated in [7], [8], [9].

focuses the signal in multiple smaller angular regions for greater spectral efficiency (SE) [3].

The beamforming architectures of multibeam antennas (MBAs) are generally divided into three categories: analog beamforming (ABF), digital beamforming (DBF), and hybrid beamforming (HBF) [4]. Fully digital MBAs (DMBAs) process beamforming in the baseband (BB) with high-precision digital signals. Each antenna element has a dedicated radio frequency (RF) chain as well as individual digitalto-analog converter (DAC) and analog-to-digital converter (ADC), thus the most flexible beamforming can be achieved. However, at mm-waves, with low power amplifier efficiency and high energy consumption of high-speed digital signal processing (DSP) chips, active arrays with a full DBF approach producing 3D adaptive multiple directional beams are not yet economically competitive [5]. Fully analog MBAs, on the other hand, suffer from large insertion and combining losses. They are also less flexible in highly dynamic and user-specific adaptation compared to DBF beamforming. A promising and feasible alternative is to use planar arrays composed of multiple vertical subarrays (a group of co-polarized antenna elements) configured with shaped and fixed analog elevation beam patterns and apply digital beamforming across multiple subarrays to generate multiple beams in the azimuth direction [5], [6]. Such an HBF structure is visualized in Fig. 1 for a dual-polarized (horizontal and vertical) active antenna system. Compared to a large array with DBF in both azimuth and elevation, its hardware complexity, power consumption, and system cost are much reduced. These apparent benefits of the proposed HBF approach bring performance trade-offs in terms of the system and user throughput, which need to be assessed under realistic 5G network deployments, user traffic scenarios, and propagation environments.

A major challenge faced when developing base stations with such HBF arrays is determining the shape of the fixed elevation beam. For example, under pure line-of-sight (LoS) propagation, a cosecant-squared beam pattern will help equalize the received power for users at different ranges [6]. However, realistic environments include multipath propagation either with or without a LoS path. Besides, the traffic distributions are typically heterogeneous

and spatially varying over time due to day-to-day business/commercial/residential dynamics and the occurrence of incidents/events. Therefore, determining a (quasi-)optimal beam shape requires in-depth system-level studies, including careful modeling of antenna subarrays with shaped elevation beam patterns, resource management schemes covering single-user/multi-user MIMO (SU/MU-MIMO) scheduling and beamforming, and assessing key performance metrics in an extensive sensitivity analysis considering e.g., different propagation environments and spatial user distributions.

The main contributions of this paper are:

- The system-level simulation (SLS) performance of HBF with a fixed and shaped elevation beam is studied for the first time.
- Inspired by daily events and festivals, a novel representation of heterogeneous traffic is presented by mixing two spatial user distributions: uniform and near-site, with weighted probability ratios.
- Several beam shapes (i.e., pencil, cosecant-squared, and flat-top beam) are compared under heterogeneous spatial traffics for the first time.
- The strategy of identifying a suitable elevation beam pattern for HBF base stations at mm-wave, depending on the spatial traffic distributions, is proposed for the first time.

The rest of the paper is organized as follows. Some of the most representative research on the performance simulation of mm-wave 5G hybrid beamforming networks is reviewed in Section II. Section III presents the communication system model, which includes distinct block diagrams and the simulation scenarios to configure radio channels. Utilizing a simulator implementation of the described model, Section IV presents and discusses the results of a range of scenario-based analyses, targeted to assess the merit of the distinct beamforming structures under different conditions. Finally, the conclusion and several promising directions for future work are provided in Section V.

II. RELATED WORK

It is a common and widely accepted approach in the wireless communications community to demonstrate proof-of-concepts at the system level via simulations by following general documents from global bodies prescribing the models, e.g., [10], [11], and [12], for use in these simulations. This is mainly because: (i) the addressed technology is not yet available in implementations; (ii) simulations allow a huge degree of flexibility in defining/considering a range of scenarios and configurations; and (iii) simulations allow us to conduct assessments much faster and therefore allow a much more thorough overall assessment with many more scenarios/configurations addressed. Many examples of specific widely requested system-level papers can be found in the literature [13], [14], [15], [16], [17], [18], [19].

To the authors' knowledge, the presented research idea on traffic-dependent optimal beam shaping in elevation for



HBF base stations is unique. However, several previous studies addressed the system performance simulation of hybrid beamforming in mm-wave 5G networks. Due to the relevance, some of the significant representatives are examined here.

The performance of conventional fully/sub-connected HBF systems is assessed in different forms e.g., in [20], [21], and [22]. In the fully connected architecture, each RF chain is connected to all antenna elements through the phase shifter network. Whereas the sub-connected structure consists of multiple subarrays and each connects to a single RF chain. These papers consider antenna designs with singlepolarization (e.g., horizontal), while two mutually orthogonal polarizations are often used to enable multilayer transmission for enhanced throughput or robustness against channel fading. Moreover, although the users are selected with sufficient angular separation for spatial multiplexing [20], [21], no scheduling algorithm (e.g., the proportional fairness (PF) scheduling [23], [24]) is applied to effectively assign radio resources to users. In addition, these papers consider only spatially uniform user distributions.

Apart from fully/sub-connected HBF techniques, a preliminary study toward assessing the system performance of HBF with a cosecant-squared elevation beam pattern is presented in [25]. However, in that research: (i) the receivers are equipped with a single isotropic antenna element, which is too idealistic, and (ii) the modeling of radio channels is much simplified by assuming that the transmission between the base station (BS) and UEs consists of a single line-of-sight (LoS) path or a single dominant non-line-of-sight (NLoS) path, without considering multipath propagation, (iii) the antenna dual-polarization, multicarrier system, multilayer transmission, and time evolution of communication channels are ignored, (iv) the co-scheduled users are randomly picked from a uniform distribution in the cell, without considering channel conditions in the co-scheduling decision. The analyses are furthermore restricted to spatially uniform traffic.

To sum up, the state-of-the-art research on system assessment of hybrid beamforming in mm-wave 5G networks uses simplistic system models. Particularly, the multilayer transmission is ignored, and the radio resource allocation mechanisms are either absent or too straightforward. Moreover, an analysis of the impact of spatially heterogeneous user distributions on the throughput performance, which is the key to our contribution, is not addressed.

We perform our system-level assessment in the most realistic way possible to us by following a well-established approach to system-level simulations and by ensuring that each component of our simulation model at the individual level is well-founded. This comprises the propagation model, antenna model, and signal model, based on [26]. In the propagation model, we utilize 3GPP-prescribed channel models implemented into QuaDRiGa by Fraunhofer [27]. The antenna model is based on the knowledge from prototyped products [6], [9]. We assume widely used and

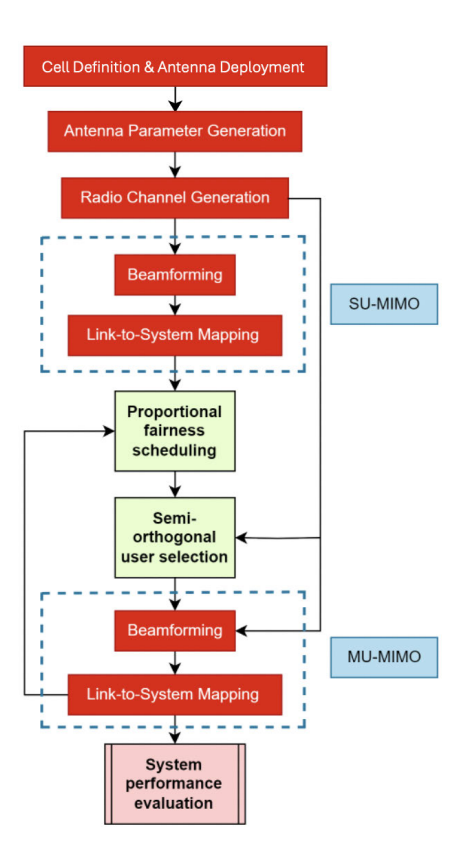


FIGURE 2. Schematic of the 5G NR SLS model, based on [26].

well-referenced models for the analog and digital precoding [28], SINR calculations [28], SINR-to-effective-SINR and SINR-to-BLER mappings [29], [30], and the scheduler [23], [24].

III. COMMUNICATION SYSTEM MODEL

The communication system model is presented in the flow chart of Fig. 2. First, the communication cell and traffic are modeled in Section III-A. Based on this, the BS antenna deployment and its vertical subarrays' analog beam configuration strategies for beam shaping are discussed in Section III-B. Next, the channel information is generated and used for digital beamforming and link-to-system mapping, in combination with advanced user scheduling and selection techniques. The signal model and resource allocation schemes describing this procedure are provided in Section III-C. Last, the simulation settings are summarized in Section III-D.

A. CELL DEFINITION, USER DISTRIBUTIONS, AND BASE STATION DEPLOYMENT

In this research, a single base station with a single array panel is deployed to serve users in a given sector of a three-sectorized site. It is assumed that the base station height is 10 meters and users are at a height of 1.5 meters [10]. The uniform user distribution is generated by placing users uniformly in the red circular service area, which models the



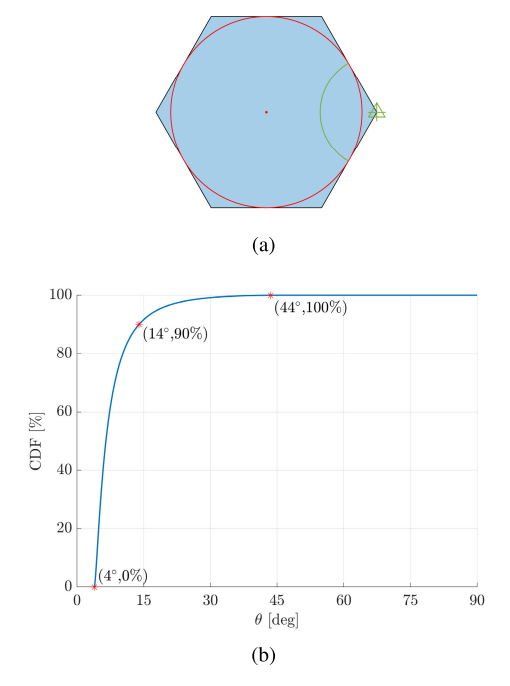


FIGURE 3. Uniform user distribution: (a) spatial layout, (b) CDF of uniformly distributed users as a function of the elevation angle.

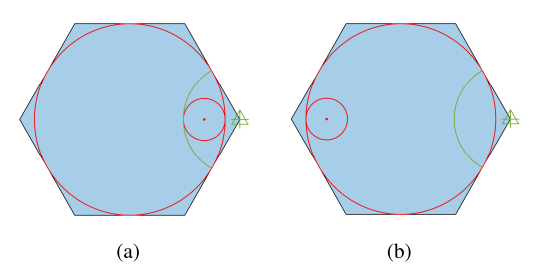


FIGURE 4. Non-uniform user distributions: (a) near-site distribution, (b) cell-edge distribution.

service area of the considered sector, shown in Fig. 3. The base station is shown with a green triangle and cross on the same figure. To configure spatially heterogeneous user distributions, the cumulative distribution function (CDF) with respect to the elevation angle θ for an assumed uniform spatial distribution of users is calculated and plotted in Fig. 3(b). Herein, the range of $\theta \in [0^{\circ}, 90^{\circ}]$ covers the region below the horizon ($\theta = 0^{\circ}$) down to the location at the foot of BS ($\theta =$ 90°). In addition, the boundary indicating the region where the 10% nearest uses are located under a uniform distribution is visualized by the green arc in Fig. 3(a). Heterogeneous user distributions characterized by an increased user density near the base station or, alternatively, near the cell egde, are proposed with the aid of Fig. 4. The assumed locations of a near-site and a cell-edge traffic hot spot are indicated in Fig. 4(a) and Fig. 4(b) respectively. Furthermore, the heterogeneous traffic distributions are also characterized by a mixing of uniform and near-site traffic, and a range of mixing ratios are considered.

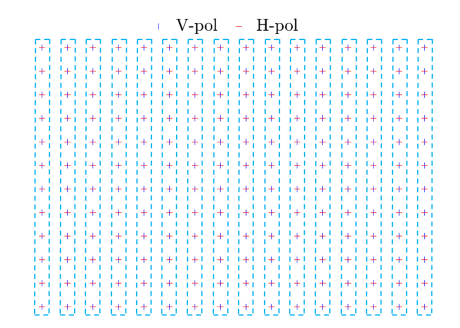
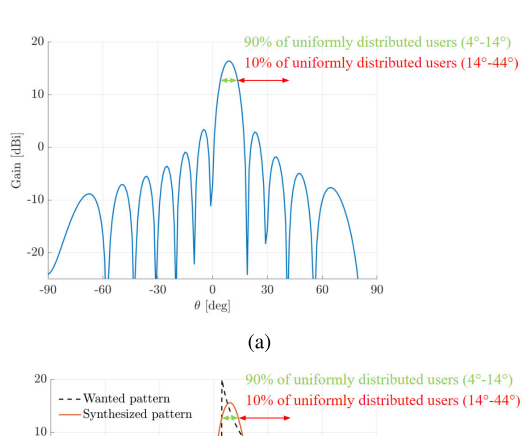
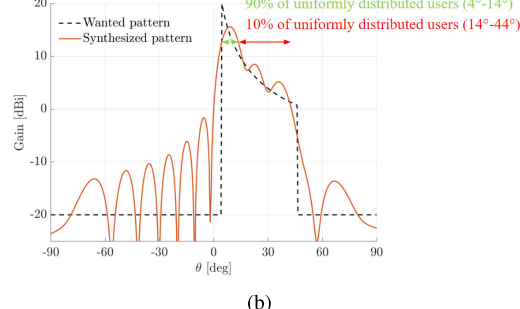


FIGURE 5. Topology of HBF beamforming structures.





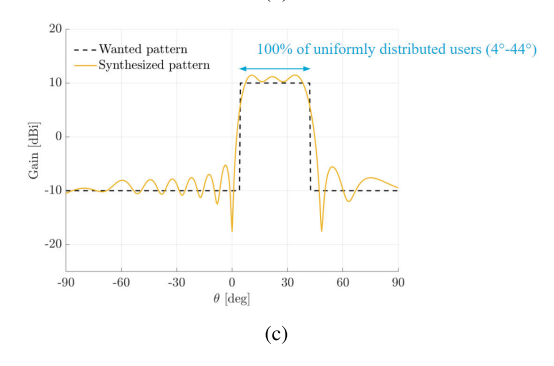


FIGURE 6. Analog elevation beam patterns under test for HBF: (a) benchmark, (b) cosecant-squared, (c) flat-top.

B. ANTENNA TOPOLOGY AND CONFIGURATION

Designed to cater to spatially heterogeneous user distributions, HBF with a pencil beam in elevation ("benchmark HBF") and two HBF with cosecant-squared and flat-top elevation beam patterns, are considered. The antenna arrays are composed of $12 \times 16 \times 2$ elements with horizontal and vertical polarizations and a half-wavelength element



spacing, which aligns well with the existing and projected size of the mm-wave massive MIMO antennas presented in the literature [31]. By grouping DBF antennas into vertical subarrays, the topology of HBF beamforming structures is shown in Fig. 5. Their analog elevation beam patterns are plotted in Fig. 6.

The "benchmark HBF" pattern is generated by feeding the antenna elements with the same amplitude and adjusting their progressive phases such that the main beam is steered to the cell edge. Its beam pattern in the elevation cut is plotted in Fig. 6(a).

To obtain the shaped beam patterns as in Fig. 6(b) and 6(c), two steps are followed. In the first step, synthesis is done by deciding on the number of antenna elements and beamforming weights. Many optimization techniques can be used for the pattern shaping purpose [32], [33]. Our technique is based on iterative rephasing and projection of the wanted pattern, which was presented in [5]. The number of elements is chosen by evaluating the trade-off between the antenna size and the deformations in the beam shape, as described in [6]. Then, in the second step, design is done by considering a series-fed antenna array, which could be based on microstrip line technology [7], [8], or waveguides with slots [9] or slots and patches [6] as radiators. The dimensions of the feeding structure and radiators are tuned at each antenna element to minimize reflections while matching the desired amplitude-phase coefficients determined in the synthesis [9]. This procedure is simulation-based and results in the fixed analog shaped beam subarray, as presented in our earlier work [6], with experimental verification of the beam patterns. We did not discuss the aspects of communication systems in that paper.

In this paper, we reuse our synthesis method in [5] with twelve elements to obtain the element excitation weights, which are then used as an input in the array factor formulation for both polarizations. The element pattern is taken as the isolated pattern of a slot antenna presented in [9], resonating at 26 GHz. The dashed lines in Fig. 6(b) and 6(c) show the idealized pattern masks, which are distorted in the realized patterns due to the limited number of antenna elements (as a compromise between the array length and gain [6]). The cosecant-squared beam pattern is designed to achieve a high gain (approx. 13 dBi) at the cell edge ($\theta = 4^{\circ}$). From the cell edge to BS ($\theta \in [4^{\circ}, 44^{\circ}]$), the antenna gain is decreased following a cosecant-squared shape to compensate for the increase of distance-based and environment-specific path gain. In the flat-top beam pattern, the gain is averaged (approx. 11 dBi) for all users within 4°-44° elevation range. Therefore, the cosecant-squared HBF focuses on cell-edge users while the flat-top HBF provides higher gain toward near-site users.

The modeling of antennas is idealized since the actual feeding, mutual coupling effects, changes in the pattern with frequency, and non-linearities caused by active circuit components are ignored. Such effects may be addressed by applying calibration techniques, as studied in [34].

Here, we propose a novel concept of beam shaping in elevation for heterogeneous traffic, and we prove our concept with quantified statistical results under a generic yet realistic array and channel model. The hardware, software, environment-specific constraints, and practical aspects can cause performance variations and changes in throughput results presented in the paper. This can be taken into account with extra design and computation complexity in the system model development if desired.

C. SIGNAL MODEL AND RESOURCE MANAGEMENT SCHEMES

It is assumed that the base station is configured with N_T transmit antennas. Each UE k is equipped with N_{R_k} antennas and $N_R = \sum_{k=1}^K N_{R_k}$ refers to the number of receive antennas of all UEs. Under the assumption of fixed-layer transmission and for now supposing that all UEs are scheduled, each UE receives L_k layers and there are in total $L = \sum_{k=1}^K L_k$ transmission layers. To extract L_k mutually orthogonal channels of each UE for beamforming [28], [35], [36], instead of the full channel matrix $\mathbf{H} \in \mathbb{C}^{N_R \times N_T}$, a reduced singular value decomposition (SVD) is applied in the following form:

$$H \approx U^{\mathsf{H}} S V$$
 (1)

Herein, $U^H \in \mathbb{C}^{N_R \times L}$ is the Hermitian conjugate of the channel left singular matrix, $S \in \mathbb{C}^{L \times L}$ is a diagonal matrix that sorts channel singular values in descending order, and $V \in \mathbb{C}^{L \times N_T}$ is the channel right singular matrix. For each UE, it is proposed to naturally choose the first L_k ($L_k \leq N_{R_k}$) vectors from $V_k \in \mathbb{C}^{N_{R_k} \times N_T}$ that corresponds to L_k strongest layers [28].

Following the flow chart of communication system model (Fig. 2), initially assuming SU-MIMO as a preparatory step feeding into the scheduler outlined below, in the "Beamforming" block, the maximum ratio transmission (MRT) precoding algorithm [28] is realized through the following rule:

$$W_{MRT} = V^{\mathsf{H}} \tag{2}$$

wherein $W_{MRT} \in \mathbb{C}^{N_T \times L}$. To enforce the transmitted power P_{tx} to be uniformly distributed over the transmission layers, each column of the precoder is normalized to have unit norm and then scaled by $\sqrt{\frac{P_{tx}}{L}}$. For each UE, the detection matrix $G_k \in \mathbb{C}^{L_k \times N_{R_k}}$ is derived using the minimum mean square error-interference rejection combining (MMSE-IRC) detection algorithm [37]:

$$G_k = (\boldsymbol{H}_k \boldsymbol{W}_k)^{\mathsf{H}} (\boldsymbol{H}_k \boldsymbol{W} (\boldsymbol{H}_k \boldsymbol{W})^{\mathsf{H}} + \lambda \boldsymbol{I})^{-1}$$
(3)

In this equation, $\boldsymbol{H}_k \in \mathbb{C}^{N_{R_k} \times N_T}$ and $\boldsymbol{W}_k \in \mathbb{C}^{N_T \times L_k}$ are the channel matrix and precoder of UE k. Each row of the detector is normalized to have unit norm. $\lambda = \frac{LP_{noise}}{P_{tx}}$ is the system noise-to-signal ratio and \boldsymbol{I} is an identity matrix of dimension $N_{R_k} \times N_{R_k}$. The MRT precoding algorithm maximizes the main lobe beamforming gain regardless of the interference, which is suitable under SU-MIMO transmission



since there is no inter-user interference. In the "Link-to-System Mapping" block, first, the SINR values per layer *l* and per physical resource block (PRB) *n* are calculated [28]:

$$SINR_{l,n} = \frac{|\mathbf{g}_{l}\mathbf{H}_{k,n}\mathbf{w}_{l}|^{2}}{\sum_{i\neq l}^{L}|\mathbf{g}_{l}\mathbf{H}_{k,n}\mathbf{w}_{i}|^{2} + P_{noise}}$$
(4)

Herein, w_l represents the lth column of W_k and g_l is the lth row of G_k . Then, the per-PRB SINRs are mapped to an effective value using the mutual information effective SINR mapping (MIESM) method [29], assuming that 256 quadrature amplitude modulation (QAM) is used. Given the block error rate (BLER) curves provided in [30], the highest modulation and coding scheme (MCS) is selected such that the BLER probability does not exceed 10%. Based on the selected MCS, the spectral efficiency is determined to calculate the bit rate of each transmission layer.

To provide a balance between the fairness and efficiency of packet scheduling, the proportional fairness (PF) scheduling algorithm [23], [24] is selected. The assumption is to schedule a candidate UE only if all its L_k layers can be scheduled. The bit rate of each scheduled UE is the sum of the per-layer bit rates. The PF scheduler is used to fairly schedule UEs while ensuring efficient resource utilization based on the PF ratio. The PF ratio is updated at each transmission time interval (TTI) and is the quotient between the instantaneous bit rate at which the UE can be potentially served in the upcoming TTI and the average throughput experienced by the UE up to and including the previous TTI. A reasonable approach to derive the upcoming instantaneous bit rate is based on SU-MIMO transmission since at this stage it is undecided which UEs will be served. After ranking UEs according to their PF ratios, the UE with the highest ratio will be scheduled first. Then, the scheduler goes through other UEs one by one and decides whether they will be co-scheduled. The decision is made based on the heuristic semi-orthogonal user selection (SUS) algorithm (adapted from [38]), which selects UEs that have sufficiently uncorrelated channels according to the orthogonality check with already scheduled layers. The sufficiency is characterized by the orthogonality threshold δ that ranges from 0 to 1. Two extreme cases are when $\delta = 0$, only the UE with the highest PF ratio is served; when $\delta = 1$, all UEs end up being scheduled. In between these extremes, δ can be tuned to optimize the cell capacity or user throughput performance.

After determining scheduled UEs, the adaptive regularized zero-forcing (ARZF) precoding algorithm [28] is chosen in the case of MU-MIMO transmission:

$$W_{ARZF} = V^{\mathsf{H}} (VV^{\mathsf{H}} + \lambda S^{-2})^{-1}$$
 (5)

Herein, λ is the system noise-to-signal ratio and λS^{-2} is the diagonal regularization matrix. The normalization is done in the same way as the MRT precoder. The ARZF precoder keeps a balance between the main lobe beamforming gain levels and inter-user interference levels. By implementing the "Beamforming" and "Link-to-System

TABLE 1. Simulation parameters (based on [6], [9], [10], [39], [40]).

Base station parameters				
Height	10 m			
Antenna model	See Section III-B			
Number of subarrays	16			
Number of antennas in a subarray	12×2			
Polarization	H/V			
Elements spacing in wavelength	0.5			
Transmitted power	188 W			
UE parameters				
Height	1.5 m			
Speed	3 km/h			
Antenna model	3GPP-3D			
Number of vertical antenna elements	2			
Number of horizontal antenna elements	2			
Polarization	H/V			
Elements spacing in wavelength	0.5			
Number of antenna elements	8			
Number of UEs	10			
Carrier parameters				
Carrier frequency	26 GHz			
Subcarrier spacing	60 kHz			
Carrier bandwidth	50 MHz			
Number of physical resource blocks	66			
Cell parameters				
Cell shape	Hexagon			
Cell range	133 m			
Other parameters				
Number of transmission layers	2			
Number of transmission time intervals	100			
Number of simulation snapshots	1000			
Propagation scenario	3GPP NR UMi LoS/NLoS			

Mapping" blocks again, the average system throughput, average user throughput, and user throughput percentile are obtained. The average system throughput is defined as the throughput that is aggregated over co-scheduled UEs and averaged over time and simulation snapshots. The average user throughput is computed by dividing the average system throughput by the number of users. The user throughput percentile represents a certain percentage in the distribution of user throughput that users experience or fall below.

D. SIMULATION SETTINGS

The simulation parameters are summarized in Table 1, which are separated into base station parameters, UE parameters, carrier parameters, cell parameters, and other parameters.

Under the 3rd generation partnership project (3GPP) standardization [10], the 3GPP NR channel model for urban micro (UMi) cell is selected with LoS and NLoS scenarios (both with multipath propagation). The BS is assumed to be equipped with an antenna array as modeled in Section III-B, with 10 meters in height [10] and a transmitted power of 188 Watts (calculated based on a per-antenna power of 27 dBm [41], [42], resulting in approximately 38 dBm power per subarray [43]). Two transmission layers (i.e., fixed-rank 2) are sent to each scheduled UE and the transmitted power is uniformly distributed among layers. The UE uses the 3GPP-3D antenna model as defined in [39]. It is equipped with a dual-polarized 2 × 2 planar array at a height of 1.5 meters [10]. In addition, to model time-evolving channels, the UE



TABLE 2. The optimal threshold δ_{opt} in distinct beamforming architectures, propagation scenarios, and user distributions.

	[LoS, Uniform]	[LoS, Near-site]	[LoS, Cell-edge]	[NLoS, Near-site]
Benchmark HBF	1	1	0.5	0
Cosecant-squared HBF	1	1	0.5	0
Flat-top HBF	1	1	0.5	0

is assumed to linearly move at a speed of 3 km/h [10] in a random direction. The 5G network is configured at the 26 GHz frequency band with a subcarrier spacing (SCS) of 60 kHz [40]. The UE channel bandwidth is set to 50 MHz with 66 PRBs based on [40]. We simulate 100 TTIs and 1000 independent snapshots considering the simulation time and accuracy. In each simulation snapshot, the UEs have a random position and movement direction, and the scatterers are randomly spaced as well.

IV. RESULTS AND DISCUSSION

The statistical results are presented and discussed in this section. To start with, in Section IV-A, a parametric study is performed to configure the user selection scheme such that it yields the best system performance. Then, the comparison among different beamforming alternatives is presented in Section IV-B, addressing various spatial user distributions in the presence of LoS multipath propagation. The performance effects under NLoS multipath propagation are discussed in Section IV-C.

A. USER SELECTION SCHEME CONFIGURATION

The configuration parameter δ (see Section III-C) of the semi-orthogonal user selection algorithm checks the channel orthogonality between candidate users and already scheduled users. We consider several options of δ , which is selected from $\{0, 0.25, 0.5, 0.75, 1\}$. The performance of the three different beamforming structures is assessed in three heterogeneous traffic and two propagation scenarios, as defined in Section III. Note that under NLoS propagation, the channel condition is much worse than the LoS case. There are no noticeable performance variations with distinct HBF structures in different user distributions. Therefore, only the results of the near-site distribution are presented.

The optimal threshold δ_{opt} in each case is the value that yields the highest average system throughput, as presented in Table 2. From the table, it is observed that the orthogonality threshold takes on different optimal values under different propagation and user distribution scenarios, indicating that the SUS user selection scheme tries to smartly schedule the users according to their channel status and optimize the degree of MU-MIMO.

In the case of [LoS, Uniform], the users are well separated with low interuser interference. In the case of [LoS, Nearsite], the users have low distance-based path loss since they are close to the BS, and the interuser interference is nulled by the grace of the ARZF precoding algorithm. Hence, the channel condition in both scenarios is acceptable to configure

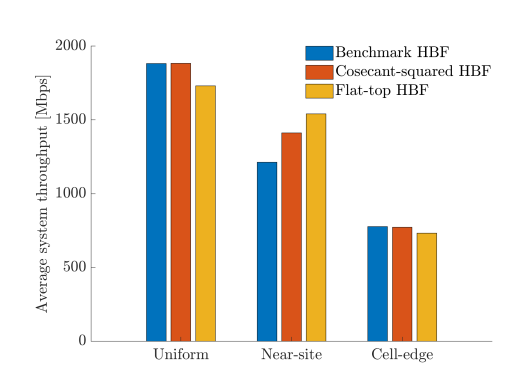


FIGURE 7. Average system throughput in the LoS scenario.

the optimal δ value to 1, indicating that all UEs are served all the time. The proposed HBF structures with fixed elevation patterns have limited beamforming flexibility and can only steer the beam in azimuth. Therefore, in the case of [LoS, Cell-edge] and [NLoS, Near-site] when the users suffer from poor channel quality due to either they are far away from the site (i.e., under cell-edge distribution) or tolerate severe signal blockage (i.e., under NLoS propagation), only the users with favorable channel condition are scheduled. The δ_{opt} is decreased to 0.5 and 0 respectively.

After configuring the user selection scheme with the optimal threshold, the performance of HBF beamforming architectures is compared in the following sections.

B. LINE-OF-SIGHT SCENARIO

The performance of deploying different HBF structures in the heterogeneous traffic and LoS scenario is assessed in this section. Firstly, the average system throughput of the three considered HBF architectures under LoS propagation in the uniform, near-site, and cell-edge user distribution, is presented in Fig. 7. In the uniform and cell-edge distributions, the cosecant-squared HBF performs similarly compared to the benchmark HBF. However, there is a performance degradation of about 8% and 6%, respectively, by using the flat-top HBF. In the near-site distribution, the performance of shaped HBF antennas is considerably higher than the benchmark. Specifically, a gain of about 16.4% (199 Mbps) and 27% (328 Mbps) is realized with the cosecant-squared and flat-top HBF respectively. The above results can be explained by looking at the elevation beam patterns of HBF as shown in Fig. 6, where shaped HBF antennas have substantially higher gain than the benchmark in the near-site distribution ($\theta \in [14^{\circ}, 44^{\circ}]$). When the users are distributed uniformly over the cell, 90% of them are served

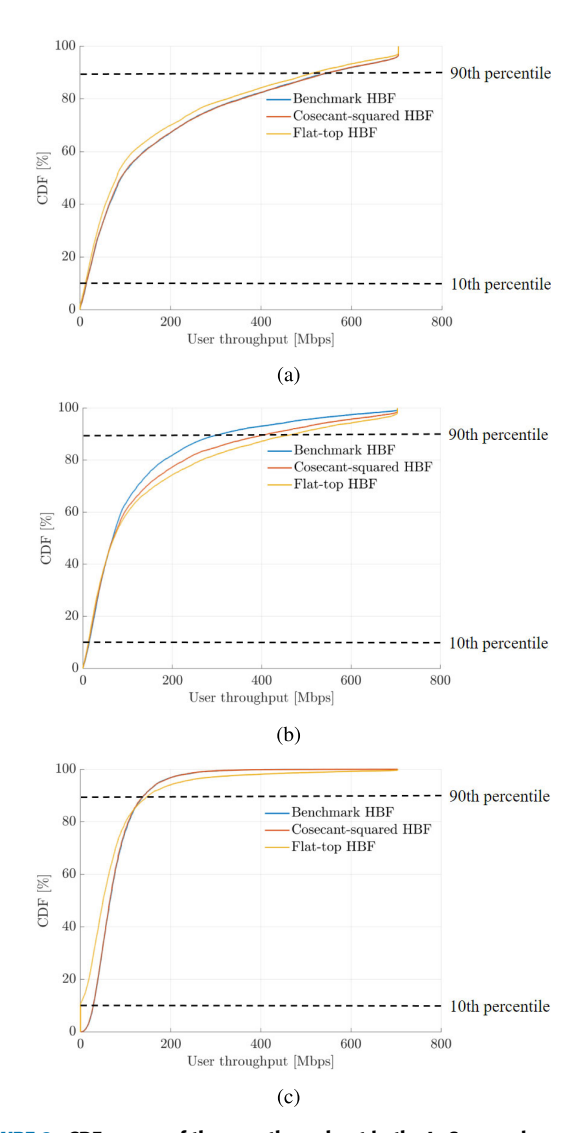


FIGURE 8. CDF curves of the user throughput in the LoS scenario: (a) uniform distribution, (b) near-site distribution, (c) cell-edge distribution.

with similar antenna gain by employing the cosecant-squared and benchmark HBF, which is higher than the gain of the flat-top HBF. The same reasoning holds for the cell-edge distribution.

Another observation in Fig. 7 is that when the users are located closer to the BS (i.e., comparing the uniform distribution to the near-site distribution), the average system throughput is dropped for all HBF antennas. This is intriguing since the propagation loss of mm-waves is less severe if the users are closer to the site, which may be intuitively expected to bring some performance improvements. The reason behind this is that in the near-site distribution, the users are distributed in a smaller area compared to the uniform distribution. Since in both distributions, all the users are co-scheduled (as explained in Section IV-A), the smaller inter-user angular spacing results in a greater sacrifice in the main lobe beamforming gain when applying the ARZF

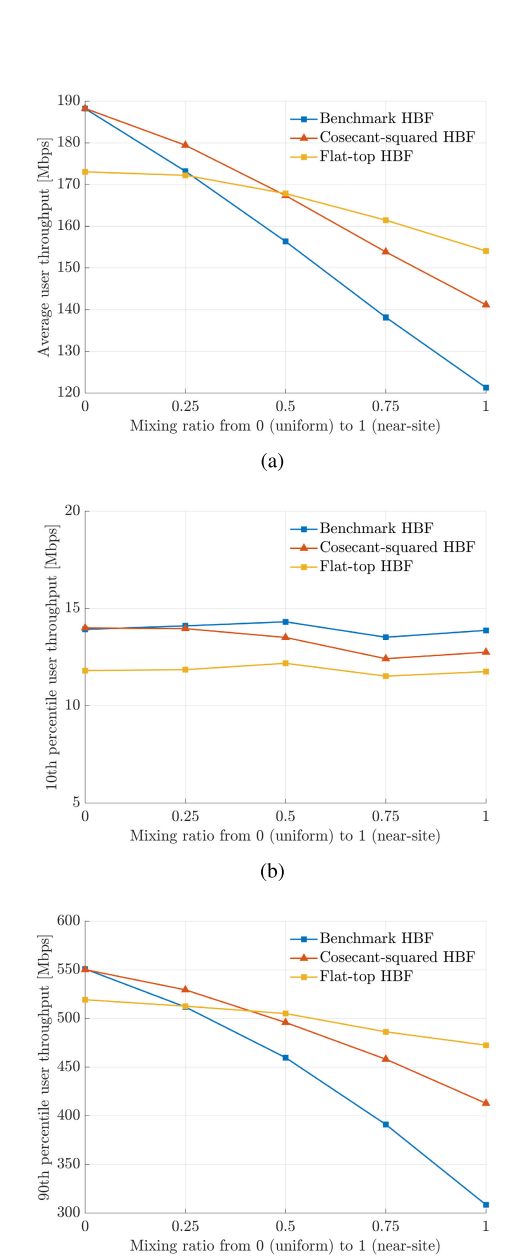


FIGURE 9. System assessment in mixed uniform and near-site distributions and the LoS scenario: (a) average user throughput, (b) 10th percentile user throughput, (c) 90th percentile user throughput.

precoding algorithm. The reduction in the beamforming gain dominates over the improvement in distance-based path loss. Therefore, the average system throughput is dropped.

Then, CDF curves of the user throughput are plotted in Fig 8. In the case of uniform distribution, the cosecant-squared HBF has a similar performance compared to the benchmark HBF, and both of them perform better than the flat-top HBF. This is due to 90% of uniformly distributed users being served with higher antenna gain using the cosecant-squared and benchmark HBF than the flat-top HBF. For the near-site distribution, the 10th percentile user throughput of shaped HBF antennas is similar



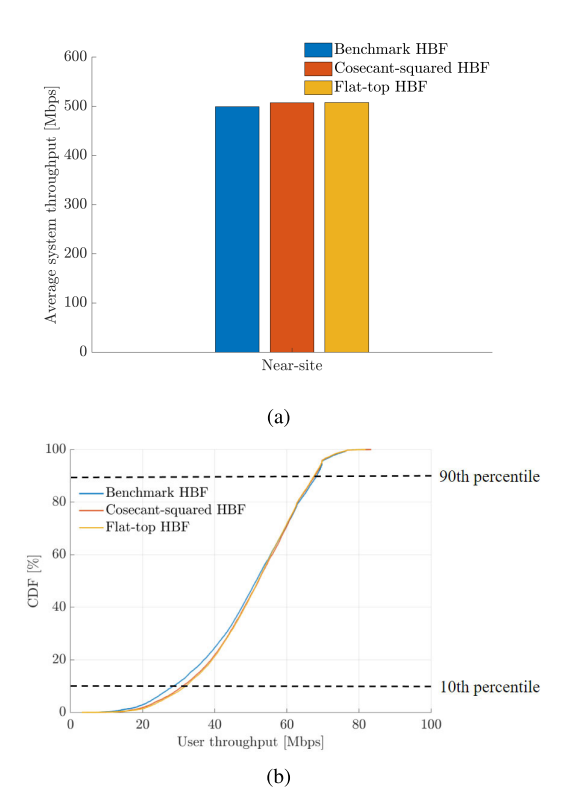


FIGURE 10. System assessment in the near-site distribution and NLoS scenario: (a) average system throughput, (b) CDF curves of the user throughput.

compared to the benchmark. However, if considering the 90th percentile user throughput, a significant performance gain of 34% (104 Mbps) and 53% (164 Mbps) exists with the cosecant-squared HBF and flat-top HBF, respectively. This shows that at the user level, shaped HBFs bring remarkable benefits for those users who have favorable channel conditions. For other users, their performance is quite similar with or without the elevation beam pattern shaping. In the case of cell-edge distribution, roughly 10.6% of the users are not served at all with the flat-top HBF, which is undesired and not fair. On the one hand, it has a lower antenna gain than the other two HBF structures. On the other hand, the users suffer from high distance-based path loss. As a result, some of the users with poor channel quality are not served.

So far, HBF with shaped elevation beam patterns show a promising performance potential in the near-site distribution. To fairly compare their performance variations, the spatially heterogeneous traffic is subsequently modeled by mixing the uniform and near-site distribution with different probabilities of occurrence. Specifically, the mixing ratio is varied between 0 (pure uniform distribution) and 1 (pure near-site distribution). The average user throughput and 10th/90th percentile user throughput in such mixed scenarios are presented in Fig. 9. Fig. 9(a) and 9(c) show a similar trend where the cosecant-squared HBF outperforms the benchmark in all mixed scenarios, except in the pure uniform distribution where they have similar performance. Their throughput

difference increases with a larger mixing ratio. For the flat-top HBF, even though it performs better than the benchmark for mixing ratios greater than 0.25, its performance degradation for lower mixing ratios is not negligible. Comparing between shaped HBF structures, the cosecant-squared HBF is better if the mixing ratio is below 0.5 when the uniform distribution has a higher probability of occurrence. On the other hand, the flat-top HBF performs better for mixing ratios greater than 0.5 when the near-site distribution occurs more often. The 10th percentile user throughput for different HBF architectures does not vary much in mixed user distributions as seen in Fig. 9(b). This is because in Fig. 8(a) and 8(b), the 10th percentile user throughput is almost the same for pure uniform and near-site distribution.

In the LoS propagation scenario, the cosecant-squared HBF shows an overall better performance than the flat-top HBF and benchmark HBF since it is more robust against differences in spatially heterogeneous traffic.

C. NON-LINE-OF-SIGHT SCENARIO

The simulation results in the NLoS scenario are discussed in this section. The average system throughput and CDF curves of the user throughput in the near-site distribution are plotted in Fig. 10. Due to severe signal blockage of mm-waves under NLoS propagation, the average system throughput drops considerably compared to the LoS case. In addition, since the direct propagation path is blocked, the shaped HBF methods do not provide significant gain anymore in terms of the average system throughput and 90th percentile user throughput. Instead, they perform similarly compared to the benchmark without any noticeable performance drop.

V. CONCLUSION

In this paper, the system performance of hybrid beamforming under spatially heterogeneous traffic and different propagation scenarios is studied for distinct analog beam shapes in elevation. The innovative research idea is to identify a suitable (in terms of the average system/user throughput and 10th/90th percentile user throughput) elevation beam pattern of HBF depending on the user distribution and propagation scenario. The performance of the considered HBF structures is simulated in spatially heterogeneous user distributions.

It is demonstrated, for the first time, that HBF with a cosecant-squared beam pattern is more robust than the flat-top HBF and the benchmark concerning differences in heterogeneous traffic. Under LoS propagation, in the near-site distribution, the cosecant-squared HBF can provide 16.4% gain in the average system throughput and 34% gain in the 90th percentile user throughput compared to the benchmark. In the uniform and cell-edge distributions, the cosecant-squared HBF performs similarly in comparison to the benchmark, while the flat-top HBF has a considerable performance degradation. In mixed uniform and near-site distributions, the flat-top HBF has a better performance than the cosecant-squared HBF for mixing ratios higher than 0.5 when the near-site distribution has more probability of



occurrence. In the NLoS scenario, the shaped HBF structures do not bring any performance disadvantages as compared to the benchmark HBF.

The suggested improvements and several promising directions for future research include: (i) modeling of the antenna mutual coupling and the beam squint [44] effect; (ii) investigating the performance potential of deploying HBF with shaped elevation beam patterns in distributed MIMO (D-MIMO); (iii) embedding reconfigurable intelligent surfaces (RISs) [45] in the NLoS scenario, which implies more deterministic modeling of the communication environment (e.g., by using ray tracing).

REFERENCES

- M. Deepender, U. Shrivastava, and J. K. Verma, "A study on 5G technology and its applications in telecommunications," in *Proc. Int. Conf. Comput. Perform. Eval. (ComPE)*, Dec. 2021, pp. 365–371.
- [2] D. M. Pozar, Microwave Engineering, 3rd ed. Hoboken, NJ, USA: Wiley, 2005.
- [3] H. Q. Ngo, E. G. Larsson, and T. L. Marzetta, "Energy and spectral efficiency of very large multiuser MIMO systems," *IEEE Trans. Commun.*, vol. 61, no. 4, pp. 1436–1449, Apr. 2013.
- [4] W. Hong, Z. H. Jiang, C. Yu, J. Zhou, P. Chen, Z. Yu, H. Zhang, B. Yang, X. Pang, M. Jiang, Y. Cheng, M. K. T. Al-Nuaimi, Y. Zhang, J. Chen, and S. He, "Multibeam antenna technologies for 5G wireless communications," *IEEE Trans. Antennas Propag.*, vol. 65, no. 12, pp. 6231–6249, Dec. 2017.
- [5] A. Roederer, J. Puskely, Y. Aslan, and A. Yarovoy, "Shaped elevation patterns for 5G base stations," in *Proc. IEEE Int. Symp. Antennas Propag.* USNC-URSI Radio Sci. Meeting (APS/URSI), Dec. 2021, pp. 795–796.
- [6] J. Puskely, T. Mikulasek, Y. Aslan, A. Roederer, and A. Yarovoy, "5G SIW-based phased antenna array with cosecant-squared shaped pattern," *IEEE Trans. Antennas Propag.*, vol. 70, no. 1, pp. 250–259, Jan. 2022.
- [7] S. Karimkashi and G. Zhang, "A dual-polarized series-fed microstrip antenna array with very high polarization purity for weather measurements," *IEEE Trans. Antennas Propag.*, vol. 61, no. 10, pp. 5315–5319, Oct. 2013
- [8] A. Vallecchi and G. B. Gentili, "Design of dual-polarized series-fed microstrip arrays with low losses and high polarization purity," *IEEE Trans. Antennas Propag.*, vol. 53, no. 5, pp. 1791–1798, May 2005.
- [9] T. Mikulasek, J. Puskely, A. G. Yarovoy, J. Lacik, and H. Arthaber, "Transverse slot with control of amplitude and phase for travelling-wave SIW antenna arrays," *IET Microw., Antennas Propag.*, vol. 14, no. 15, pp. 1943–1946, Dec. 2020.
- [10] Study on Channel Model for Frequencies From 0.5 to 100 GHz, Standard 3GPP TR 38.901 v18.0.0, 2024.
- [11] Guidelines for Evaluation of Radio Interface Technologies for IMT-Advanced, document Report ITU 638, 2009.
- [12] N. Alliance, "Next generation mobile networks radio access performance evaluation methodology," Version 1.0, NGMN Alliance e.V., Düsseldorf, Germany, White Paper, Jan. 2008.
- [13] S. Suyama, T. Okuyama, N. Nonaka, and T. Asai, "Recent studies on massive MIMO technologies for 5G evolution and 6G," in *Proc. IEEE Radio Wireless Symp. (RWS)*, Jan. 2022, pp. 90–93.
- [14] J. Jeon, G. Lee, A. A. I. Ibrahim, J. Yuan, G. Xu, J. Cho, E. Onggosanusi, Y. Kim, J. Lee, and J. C. Zhang, "MIMO evolution toward 6G: Modular massive MIMO in low-frequency bands," *IEEE Commun. Mag.*, vol. 59, no. 11, pp. 52–58, Nov. 2021.
- [15] M. Polese, M. Giordani, T. Zugno, A. Roy, S. Goyal, D. Castor, and M. Zorzi, "Integrated access and backhaul in 5G mmWave networks: Potential and challenges," *IEEE Commun. Mag.*, vol. 58, no. 3, pp. 62–68, Mar. 2020.
- [16] C.-P. Li, J. Jiang, W. Chen, T. Ji, and J. Smee, "5G ultra-reliable and low-latency systems design," in *Proc. Eur. Conf. Netw. Commun.* (EuCNC), Jun. 2017, pp. 1–5.
- [17] M. Fuentes, J. L. Carcel, C. Dietrich, L. Yu, E. Garro, V. Pauli, F. I. Lazarakis, O. Grøndalen, Ö. Bulakci, J. Yu, W. Mohr, and D. Gomez-Barquero, "5G new radio evaluation against IMT-2020 key performance indicators," *IEEE Access*, vol. 8, pp. 110880–110896, 2020.

- [18] Y. R. Li, M. Chen, J. Xu, L. Tian, and K. Huang, "Power saving techniques for 5G and beyond," *IEEE Access*, vol. 8, pp. 108675–108690, 2020.
- [19] R. Maldonado, A. Karstensen, G. Pocovi, A. A. Esswie, C. Rosa, O. Alanen, M. Kasslin, and T. Kolding, "Comparing Wi-Fi 6 and 5G downlink performance for industrial IoT," *IEEE Access*, vol. 9, pp. 86928–86937, 2021.
- [20] T. Kuehne, X. Song, G. Caire, K. Rasilainen, T. H. Le, M. Rossi, I. Ndip, and C. Fager, "Performance simulation of a 5G hybrid beamforming millimeter-wave system," in *Proc. WSA 24th Int. ITG Workshop Smart Antennas*, Feb. 2020, pp. 1–6.
- [21] X. Song, T. Kühne, and G. Caire, "Fully-/partially-connected hybrid beamforming architectures for mmWave MU-MIMO," *IEEE Trans. Wireless Commun.*, vol. 19, no. 3, pp. 1754–1769, Mar. 2020.
- [22] S. Wan, H. Zhu, K. Kang, and H. Qian, "On the performance of fully-connected and sub-connected hybrid beamforming system," *IEEE Trans. Veh. Technol.*, vol. 70, no. 10, pp. 11078–11082, Oct. 2021.
- [23] Y. Barayan and I. Kostanic, "Performance evaluation of proportional fairness scheduling in LTE," in *Proc. World Congr. Eng. Comput. Sci.*, vol. 2, 2013, pp. 712–717.
- [24] A. M. Nor, O. Fratu, S. Halunga, A. Alyosef, Z. D. Zaharis, S. Rizou, and P. I. Lazaridis, "Demand based proportional fairness scheduling for 5G eMBB services," in *Proc. IEEE Int. Black Sea Conf. Commun. Netw. (BlackSeaCom)*, Jun. 2022, pp. 263–268.
- [25] S. Salman, Y. Aslan, J. Puskely, A. Roederer, and A. Yarovoy, "System modeling and simulation in 5G: A hybrid beamforming approach with power flux equalization in the elevation plane," in *Proc. 49th Eur. Microw. Conf. (EuMC)*, Oct. 2019, pp. 746–749.
- [26] W. Chen, "System performance evaluation of hybrid beamforming with shaped beam patterns for mm-wave 5G base stations," M.S. thesis, Dept. Microelectronics, Delft Univ. Technol., Delft, The Netherlands, 2023. [Online]. Available: http://resolver.tudelft.nl/uuid:95d057d5-524c-4776-9a22-8869d2bd2c56
- [27] QuaDRiGa: The Next Generation Radio Channel Model. Accessed: Jun. 26, 2024. [Online]. Available: https://quadriga-channel-model.de/
- [28] E. Bobrov, B. Chinyaev, V. Kuznetsov, H. Lu, D. Minenkov, S. Troshin, D. Yudakov, and D. Zaev, "Adaptive regularized zero-forcing beamforming in massive MIMO with multi-antenna users," 2021, arXiv:2107.00853.
- [29] E. Tuomaala and H. Wang, "Effective SINR approach of link to system mapping in OFDM/multi-carrier mobile network," in Proc. 2nd Asia–Pacific Conf. Mobile Technol., Appl. Syst., 2005, p. 5.
- [30] I. Kim, J. Um, and S. Park, "Implementation and performance evaluation of 256-QAM in Vienna system level simulator," in *Proc. 20th Int. Conf.* Adv. Commun. Technol. (ICACT), Feb. 2018, pp. 556–559.
- [31] P. Hindle, "Comprehensive survey of commercial mmWave phased array companies," *Microw. J.*, Jan. 2020. [Online] Available: https: //www.microwavejournal.com/ar9cles/33357-comprehensivesurvey-of-commercial-mmwave-phased-array-comp
- [32] R. Elliott and G. Stern, "A new technique for shaped beam synthesis of equispaced arrays," *IEEE Trans. Antennas Propag.*, vol. AP-32, no. 10, pp. 1129–1133, Oct. 1984.
- [33] O. M. Bucci, G. Franceschetti, G. Mazzarella, and G. Panariello, "A general projection approach to array synthesis," in *Dig. Antennas Propag. Soc. Int. Symp.*, Jun. 1989, pp. 146–149.
- [34] Y. Aslan, P. Aubry, N. B. Onat, J. Janssen, M. Geurts, and A. Yarovoy, "Heuristic over-the-air calibration of beamformer ICs in active mm-wave phased arrays," in *Proc. IEEE Conf. Antenna Meas. Appl. (CAMA)*, Nov. 2023, pp. 840–845.
- [35] L. Sun and M. R. McKay, "Eigen-based transceivers for the MIMO broadcast channel with semi-orthogonal user selection," *IEEE Trans. Signal Process.*, vol. 58, no. 10, pp. 5246–5261, Oct. 2010.
- [36] G. Lebrun, T. Ying, and M. Faulkner, "MIMO transmission over a time-varying channel using SVD," in *Proc. Global Telecommun. Conf.* (GLOBECOM), vol. 1, Mar. 2002, pp. 414–418.
- [37] B. Ren, Y. Wang, S. Sun, Y. Zhang, X. Dai, and K. Niu, "Low-complexity MMSE-IRC algorithm for uplink massive MIMO systems," *Electron. Lett.*, vol. 53, no. 14, pp. 972–974, Jul. 2017.
- [38] S. Braam, R. Litjens, P. Smulders, and W. IJntema, "Assessment of distributed multi-user MIMO transmission in 5G networks," in *Proc. 18th* ACM Symp. Mobility Manage. Wireless Access, Nov. 2020, pp. 125–132.
- [39] Study on 3D Channel Model for LTE, Standard 3GPP TR 36.873 v12.5.0,
- [40] User Equipment (UE) Radio Transmission and Reception; Part 2: Range 2 Standalone, Standard 3GPP TS 38.101-2 v16.4.0, 2020.



- [41] Z. Wang, S. Hu, L. Gu, and L. Lin, "Review of Ka-band power amplifier," Electronics, vol. 11, no. 6, p. 942, Mar. 2022.
- [42] J. Curtis, A.-V. Pham, and F. Aryanfar, "Ka-band Doherty power amplifier with 26.9 dBm output power, 42% peak PAE and 32% back-off PAE using GaAs PHEMTS," IET Microw., Antennas Propag., vol. 10, no. 10, pp. 1101-1105, Jul. 2016.
- [43] X. Liu, X.-W. Zhu, Z.-M. Zhao, and R.-J. Liu, "A three-stage 6W GaN power combining amplifier MMIC design at Ka-band," in Proc. Int. Conf. Microw. Millim. Wave Technol. (ICMMT), Aug. 2022, pp. 1-3.
- [44] L. Afeef and H. Arslan, "Beam squint effect in multi-beam mmWave massive MIMO systems," in Proc. IEEE 96th Veh. Technol. Conf. (VTC-Fall), Sep. 2022, pp. 1-5.
- [45] C. Pan, H. Ren, K. Wang, J. F. Kolb, M. Elkashlan, M. Chen, M. Di Renzo, Y. Hao, J. Wang, A. L. Swindlehurst, X. You, and L. Hanzo, "Reconfigurable intelligent surfaces for 6G systems: Principles, applications, and research directions," IEEE Commun. Mag., vol. 59, no. 6, pp. 14-20, Jun. 2021.



WENXU CHEN received the dual B.Sc. degree in mechatronics engineering from the HZ University of Applied Sciences, The Netherlands, and Shanghai Maritime University, China, in 2020, and the M.Sc. degree in electrical engineering from Delft University of Technology, The Netherlands, in 2023. Following his master's study, he was employed as a System Engineer with Valeo. His current research and development covers the electromagnetic (EM) performance simulation of

the integration of cutting-edge automotive radars, which greatly reduces the risk of radar underperformance before the start of production (SOP) of vehicles.



VOLUME 13, 2025

YANKI ASLAN received the B.Sc. degree with double specialization in communications and microwaves/antennas from the Department of Electrical and Electronic Engineering, Middle East Technical University, Ankara, Türkiye, in 2014, and the M.Sc. and Ph.D. degrees (cum laude) in electrical engineering from Delft University of Technology (TU Delft), Delft, The Netherlands, in 2016 and 2020, respectively. Following his postdoctoral research with the

Microwave Sensing, Signals and Systems (MS3) Group, TU Delft, he started as an Assistant Professor with TU Delft, in April 2021. His current research interests include phased arrays for next-generation communication and sensing systems, array optimization, multibeam antennas, front-end architectures, and beamforming algorithms. He was one of the recipients of the IEEE AP-S Doctoral Research Grant, in 2018, and the EuMA Internship Award, in 2019.



REMCO LITJENS received the M.Sc. degree (Hons.) in econometrics from Tilburg University, The Netherlands, in 1994, the M.Sc. degree in electrical engineering and computer sciences from the University of California at Berkeley, USA, in 1996, and the Ph.D. degree in applied mathematics from the University of Twente, The Netherlands, in 2003. While employed as a Technical Scientific Researcher with KPN Research, The Netherlands, he started his part-

time Ph.D. research at the University of Twente. As of 2003, he is employed as a Senior Scientist with TNO, The Netherlands, while since 2014 also holding a part-time associate professorship at Delft University of Technology, The Netherlands. His core expertise is on the development, assessment, planning, and (self-)optimization of mobile/wireless networking technologies. He has served on the project board for the European projects SOCRATES and SEMAFOUR, on the management committees for COST 279 and COST 290, as well as on several technical program committees for international conferences and workshops. He has published over 100 articles in journals, magazines, and conference proceedings (with best-paper awards received at WWIC 2008, WCNC 2014, and EuCNC 2015). He is a co-inventor of over 25 granted or filed patents, and has written/contributed to five books.



ALEXANDER YAROVOY (Fellow, IEEE) received the Diploma degree (Hons.) in radiophysics and electronics from Kharkov State University, Ukraine, in 1984, and the Candidate Physics and Mathematical Sciences and the Doctor Physics and Mathematical Sciences degrees in radiophysics, in 1987 and 1994, respectively. In 1987, he joined the Department of Radiophysics, Kharkov State University, as a Researcher, where he became a Full Professor, in 1997. From September 1994 to

September 1996, he was with the Technical University of Ilmenau, Germany, as a Visiting Researcher. Since 1999, he has been with Delft University of Technology, The Netherlands. He has authored and co-authored more than 500 scientific or technical papers, seven patents, and 15 book chapters. His current research interests include high-resolution radar, microwave imaging, and applied electromagnetics (in particular, UWB antennas). He was a recipient of the European Microwave Week Radar Award for the paper that best advances the state-of-the-art in radar technology, in 2001 (together with L. P. Ligthart and P. van Genderen), and in 2012 (together with T. Savelyev). In 2010 together with D. Caratelli, he got the Best Paper Award of the Applied Computational Electromagnetic Society (ACES). Since 2009, he has been the Chair of the Microwave Sensing, Systems and Signals Group. He served as the General TPC Chair for the 2020 European Microwave Week (EuMW 2020), the Chair and the TPC Chair for the Fifth European Radar Conference (EuRAD 2008), and the Secretary for the First European Radar Conference (EuRAD 2004). He also served as the Co-Chair and the TPC Chair for the Tenth International Conference on GPR (GPR 2004). He served as an Associate Editor for IEEE Transactions on Radar Systems and the International Journal of Microwave and Wireless Technologies, from 2011 to 2018. From 2008 to 2017, he was the Director of the European Microwave Association (EuMA).

125943